Convection with internal heat sources and thermal turbulence in the Earth's mantle

Bryan Travis[1] and Peter Olson[2]

[1] *Earth and Environmental Sciences Division, Los Alamos National Laboratory, Los Alamos, NM 87545, USA*
[2] *Department of Earth and Planetary Sciences, The Johns Hopkins University, Baltimore, MD 21218, USA*

SUMMARY

The influence of internal heat sources on mantle convection is investigated using numerical calculations of 2-D thermal convection in an infinite Prandtl number, incompressible fluid. The geometry is a cylindrical annulus with inner and outer radii in proportion to the whole mantle. Time-dependent calculations are made starting from random initial conditions, with Rayleigh numbers Ra_T (based on boundary-temperature difference) and Ra_H (based on internal-heat production) in the range $10^3 \leq Ra_T \leq 10^7$ and $0 \leq Ra_H \leq 24\,Ra_T$. At fixed Ra_T, increasing Ra_H results in transitions in flow structure from steady cells, to a pattern of stationary cells with time-variable amplitude, and finally to thermally turbulent convection with a non-stationary cell count. For $Ra_T < 10^5$, the equilibrium cell-aspect ratio increases with Ra_H, from near unity (10-cell solution) at $Ra_H = 0$ to three (four-cell solution) at $Ra_H = 8Ra_T$. Above $Ra_T = 10^5$, the flow is fully time dependent and consists of unequal, non-stationary cells separated by migrating boundaries. Recurring plumes develop from instabilities in both the surface and the basal boundary layers, travel with and modify the large-scale circulation. For $Ra_T > 10^5$ and $Ra_H > Ra_T$ approximately, the travelling plumes disrupt the large-scale circulation, producing turbulent convection. At $Ra_T = 10^7$ the flow is fully developed thermal turbulence, and for $Ra_H > 0$, consists of a rapidly fluctuating, irregular flow driven by transient rising and sinking sheets of buoyant fluid. Large fluctuations in total kinetic energy occur in this regime, with periodicities ranging from 40 to 1400 Myr. The transition to thermal turbulence occurs in these calculations at Rayleigh numbers well below the value estimated for subsolidus convection in the mantle, suggesting thermally turbulent convection may occur in the mantle, a consequence of internal heat sources. Thermal turbulence offers an explanation for long-term fluctuations in the rate of subduction, sea-floor spreading and global volcanic activity.

Key words: annulus, convection, Earth's mantle, internal heating, turbulence.

1 INTRODUCTION

Subsolidus mantle convection is usually modelled as thermal convection in an infinite Prandtl number fluid. For whole-mantle convection, the flow is assumed to be driven by a combination of basal heat from the core and volumetrically distributed heat sources. At low Rayleigh numbers, thermal convection in such a fluid consists of spatially periodic, steady-state cells. Experiments on plane-layer convection in high Prandtl number fluids (Whitehead & Parsons 1978; Krishnamurti 1970; White 1988) and 3-D calculations of convection in infinite Prandtl number fluids (Travis, Olson & Schubert 1990) demonstrate

that as the Rayleigh number is increased, a sequence of transitions occurs, first to steady 3-D flow, then to time-dependent flow. Further increases in Rayleigh number amplify the degree of time dependence, eventually leading to a form of thermal turbulence. Thermal turbulence in a fluid with an effectively infinite Prandtl number (in which the inertia is negligible) is a phenomenon of considerable interest in fluid mechanics. In this regime, periodicity and closed cells are absent, the instantaneous cell boundaries fluctuate with velocities nearly as great as the fluid velocity, disconnected thermals replace continuous thermal plumes, and there are large-amplitude variations in total kinetic energy and heat flux.

1

It has been suggested that at least two distinct forms of turbulence occur in thermal convection, the so-called 'soft' and 'hard' regimes. This division has proved useful for rationalizing the spectra of temperature fluctuations obtained from laboratory experiments using moderate Prandtl number fluids (Castaing *et al.* 1989; Solomon & Gollub 1991). Recently, Yuen *et al.* (1993) have proposed a similar division for infinite Prandtl number fluid convection. According to these authors, the transition from soft to hard turbulence is determined by the appearance of discontinuous thermals and also by the development of a flat portion of the temperature fluctuation spectrum, both of which occur above a certain Rayleigh number.

Previous laboratory and numerical experiments demonstrate the transition to 'soft' thermal turbulence occurs at a Rayleigh number of approximately 10^6 (Whitehead & Parsons 1978; Hansen, Yuen & Kroening 1990; Solheim & Peltier 1990). For whole-mantle convection, the Rayleigh number based on the superadiabatic temperature increase across the mantle is in the neighbourhood of 10^7 (Olson 1987), suggesting that at least the 'soft' form of thermal turbulence is possible.

Mantle convection is considerably more complicated than simple Rayleigh–Benard convection in a homogeneous fluid. One important difference is that the mechanically strong lithosphere tends to suppress instabilities of the top boundary layer, an effect which retards the onset of time dependence in convection. Davies (1988) has argued that the constraint of surface plate motion impedes the development of thermal turbulence in the mantle. Another difference is that mantle convection is 3-D, whereas most of the high Rayleigh number calculations used to simulate mantle convection are 2-D. The dimensionality of the flow affects appearance of turbulence. For example, in base-heated Rayleigh–Benard convection, time-dependent, 2-D large-aspect ratio rolls are unstable to steady-state 3-D planforms at Rayleigh numbers $Ra_T \leq 10^5$ (Travis *et al.* 1990). In general, the geometrical restrictions imposed by two-dimensionality tend to produce time dependence at lower Rayleigh numbers than in naturally occurring 3-D convection.

Other properties of mantle convection promote time dependence. Among these are compressibility (Machetel & Yuen 1989), sphericity (Bercovici, Schubert & Glatzmaier 1989) and non-Newtonian (power-law) rheology (Christensen & Yuen 1989; Malevsky & Yuen 1992). But the property receiving the most attention, in this context, is the endothermic phase transformation at 660 km depth. The results of numerous calculations of thermal convection in the presence of an endothermic phase transformation with a negative Clapeyron slope equal to the experimentally determined value for perovskite-forming reactions show increased time dependence, compared to the same calculation without the phase transformation (Machetel & Weber 1991; Peltier & Solheim 1992; Weinstein 1993; Tackley *et al.* 1993). In these calculations, the flow is episodic, with quiet periods, characterized by low kinetic energy, low heat flow and layered convective structure, alternating with active periods, when the flow is continuous across the phase boundary and the kinetic energy and heat flow are high. The transition from quiet to active periods occurs when the internal thermal boundary layer, which

develops at the phase transition during the layered period, becomes unstable.

We do not consider the contributions to time dependence from non-linear rheology or phase transformations in this paper, not because they are negligible in the mantle, but simply for the purpose of isolating the role of internal heat generation. By focusing on just the influence of internal heat sources, we show how the presence of even small amounts of internal heat sources precipitates time dependence in thermal convection, and that the Rayleigh number at which the transition to thermal turbulence occurs decreases with increasing heat-source concentration. We find large-amplitude fluctuations in globally averaged properties such as total kinetic energy and heat flux occur simply from the presence of internal heat generation, without any contribution from phase transitions.

The generation of time dependence by internal heat sources in 2-D models of mantle convection is already well established (McKenzie, Roberts & Weiss 1974; Jarvis 1984; Schubert & Anderson 1985; Machetel & Yuen 1987, 1989; Weinstein, Olson & Yuen 1989; Solheim & Peltier 1990). Previous calculations of 2-D convection within rectangular boxes in the time-dependent regime have demonstrated that the onset of thermal turbulence is delayed by the reflection condition imposed by the vertical sidewalls. For example, Jarvis (1984) found that steady-state solutions persist in square (unit aspect ratio) boxes up to $Ra = 10^8$ with base heating and free-slip boundaries. It is now understood that the onset of time dependence occurs in 2-D, plane-layer convection at rather low Rayleigh numbers as a bifurcation from steady-state large-aspect ratio (elongated) cells (Hansen & Ebel 1988; Christensen 1987; Vincent & Yuen 1988; Weinstein *et al.* 1989). It is also known that a large-aspect ratio computational domain is needed in order to properly simulate the transition to thermal turbulence (Hansen *et al.* 1990). Internal heat generation also promotes time dependence 3-D convection. This has been demonstrated both in laboratory experiments (Weinstein & Olson 1990) and in calculations (Houseman 1988; Bercovici *et al.* 1989; Travis, Weinstein & Olson 1990; Tackley *et al.* 1993).

Time-dependent calculations of mantle convection ideally should be done in the 3-D spherical-shell geometry of the mantle. Only recently have the computer resources become available to permit a systematic numerical study of the transition to thermal turbulence in a full spherical shell (Tackley *et al.* 1993). With this limitation in mind, we have chosen to make our calculations in a 2-D cylindrical annulus. Preserving two-dimensionality allows for enough resolution in the numerical grid to reach Rayleigh numbers in excess of 10^7, the regime where fully developed thermal turbulence occurs. In addition, the annular geometry incorporates curvature and connectedness, two important aspects of the spherical mantle. This geometry has been used previously to investigate the effects of plates on the pattern of mantle convection and mantle heterogeneity (Gurnis & Zhong 1991).

2 EQUATIONS OF MOTION AND NUMERICAL SOLUTION

The conservation equations for momentum, mass, and heat for thermal convection in a Boussinesq, infinite Prandtl

number fluid are, in dimensionless form

$$\nabla^2 \mathbf{u} = \nabla P - \hat{\mathbf{r}} Ra_T T \tag{1}$$

$$\nabla \cdot \mathbf{u} = 0 \tag{2}$$

$$\frac{dT}{dt} = \nabla^2 T + \frac{Ra_H}{Ra_T}. \tag{3}$$

Heating is specified by two Rayleigh numbers. The first is based on the temperature difference across the annulus

$$Ra_T = \frac{\alpha g \Delta T D^3}{\kappa \nu} \tag{4}$$

and the second based on the density of internal heat sources, H

$$Ra_H = \frac{\alpha g H D^5}{C_p \kappa \mu}. \tag{5}$$

Here $\mathbf{u}$ is fluid velocity, P is pressure, T is temperature, t is time, α is thermal expansivity, g is the acceleration of gravity in the radial direction $\hat{\mathbf{r}}$, C_p is specific heat, κ is thermal diffusivity, ν is kinematic viscosity, μ is dynamic viscosity, and $D = r_c - r_i$ is the thickness of the annulus. The equations (1–3) are non-dimensionalized using D, D^2/κ and ΔT as units of length, time and temperature, respectively.

In cylindrical coordinates (r, θ, z), the curl of the momentum equation (1) is, in terms of the stream-function ψ and the z component of vorticity ω

$$\nabla^2 \omega = Ra_T \frac{\partial T}{\partial \theta} \tag{6}$$

and

$$\nabla^2 \psi = -\omega \tag{7}$$

in which

$$\mathbf{u} = \nabla \times (\hat{\mathbf{z}} \psi) = \frac{\hat{\mathbf{r}}}{r} \frac{\partial \psi}{\partial \theta} - \hat{\boldsymbol{\theta}} \frac{\partial \psi}{\partial r} \tag{8}$$

are the components of velocity.

The boundary conditions on the inner and outer surfaces are constant temperature, impermeable and stress free. These can be written as

$$\psi = \omega = 0, \qquad T = 1; \qquad r = r_i = 0.55 \tag{9}$$

$$\psi = \omega = 0, \qquad T = 0; \qquad r = r_c = 1. \tag{10}$$

Equations (3–10) are solved by finite difference. The mesh consists of cells with uniform radial and angular dimensions Δr, $\Delta \theta$. Stream function and vorticity are evaluated at the grid-cell corners, while temperature is evaluated at grid-cell centres. Temperature is advanced in time by an explicit method, using the Courant condition to determine the time step Δt, with the velocities calculated from (8) using centred difference approximations applied to the stream function from the previous time step. Advection and diffusion of temperature are calculated in terms of surface integrals of flux evaluated over each cell. In these integrals, temperature and velocity are expressed as quadratic and linear functions, respectively, over each cell face (Travis 1990). Forward-time differencing of (3) introduces diffusion-like terms, which are negative valued and which limit the time step Δt and reduce accuracy in time

to $O(\Delta t)$. A more accurate analysis of the truncation error terms in time (Ramshaw & Dukowicz 1979) results in a modified difference equation that includes a tensor diffusivity term, reducing numerical dispersion and providing $O(\Delta t^2)$ accuracy. Once the temperature field is advanced, eqs (6) and (7) are then solved with the NCAR Poisson equation solver (Swarztrauber & Sweet 1975), using the new temperature field. Initial conditions consist of uniformly distributed random temperatures selected from the interval (0.49–0.51), so that the average initial temperature approximates the mean of the boundary temperatures. Numerical grid size, Rayleigh number, and duration of all calculations are listed in Table 1. The duration of each calculation depends on the rate of approach to statistical thermal equilibrium, which depends on grid size and Rayleigh number. Particularly in cases with internal heat sources, it is not possible to accurately determine the equilibrium average temperature *a priori*. Most calculations exhibit an initial adjustment period during which the average temperature approaches a stationary equilibrium value. The duration of this adjustment period decreases with increasing Rayleigh number. It is typically one diffusion time unit for Rayleigh numbers near 10^4, decreases to about 0.05 at Rayleigh numbers above 10^6, and increases with increasing internal heat content. All

Table 1. Calculation parameters.

Ra_T	Ra_H	Grid	Duration	Result
1×10^4	0	16×128	2.0	SS,10
1×10^4	1×10^4	16×128	2.0	SS,8
1×10^4	2×10^4	16×128	2.0	OS,6
1×10^4	4×10^4	16×128	2.0	OS,6
3.2×10^4	0	32×256	2.0	SS,8
3.2×10^4	3.2×10^4	32×256	1.2	OS,8
3.2×10^4	6.4×10^4	32×256	1.2	OS,6
3.2×10^4	9.6×10^4	32×256	1.0	OS,4
3.2×10^4	1.28×10^5	32×256	2.3	BLI,4
3.2×10^4	2.56×10^5	32×256	1.4	BLI,4
1×10^5	0	32×256	1.6	OS,6
1×10^5	1×10^5	32×256	2.4	BLI,6
1×10^5	2×10^5	32×256	2.4	BLI,6
1×10^5	4×10^5	32×256	2.4	BLI,6
1×10^5	6×10^5	32×256	2.4	MCT
3.2×10^5	0	48×384	0.16	BLI,8
3.2×10^5	3.2×10^5	48×384	0.16	BLI,8
3.2×10^5	6.4×10^5	48×384	0.16	MCT
3.2×10^5	1.28×10^6	48×384	0.16	MCT
3.2×10^5	2.56×10^6	48×384	0.16	MCT
1×10^6	0	64×512	0.07	BLI,8
1×10^6	1×10^6	64×512	0.07	MCT
1×10^6	2×10^6	64×512	0.07	MCT
1×10^6	4×10^6	64×512	0.07	MCT
1×10^7	0	96×768	0.02	MCT
1×10^7	6×10^7	128×1024	0.05	MCT
1×10^7	24×10^7	128×1024	0.05	MCT

Regimes: SS = steady state; OS = oscillatory; BLI = boundary-layer instability; MCT = multicell turbulent; number denotes equilibrium cell count.

calculations presented in this paper were continued until the average temperature became statistically stationary at the 0.1 per cent level or better. In addition to average temperature, we have monitored the volume-averaged kinetic energy, defined as

$$E = \frac{1}{2A} \int_0^{2\pi} \int_{r_i}^{r_c} (\mathbf{u} \cdot \mathbf{u}) r \, dr \, d\theta \tag{11}$$

where $A = 2\pi(r_c^2 - r_i^2)$ is the area of the annulus, and the Nusselt number, defined at any radius r as

$$Nu = \frac{1}{2\pi r} \int_0^{2\pi} \left(\frac{\partial \psi}{\partial \theta} T - r \frac{\partial T}{\partial t} \right) d\theta. \tag{12}$$

3 EQUILIBRIUM FLOW REGIMES

The majority of the cases listed in Table 1 are intrinsically time dependent, and achieve equilibrium only in a time-averaged, statistical sense. It is difficult to determine just when equilibrium defined this way is reached, because many of these cases evolve toward equilibrium through transient, intermediate states, which may persist for a long time. For example, the initial planform in many of the cases in Table 1 is a 10-cell or a 12-cell planform, produced by instability of growing surface and basal thermal boundary layers. The 10- or 12-cell configurations often persist for several overturns as quasi-steady states, but eventually they become unstable to larger aspect ratio cell configurations. Long-lived, transient initial states often occur in calculations with internal heat sources. Accordingly, we have adopted several criteria for judging the approach to equilibrium. In cases with internal heat generation, equilibration of the

mean (volume-averaged) temperature is the simplest criterion. For the purely base-heated cases, the average temperature may remain stationary even as the planform changes, and so for those cases, convergence to a stationary Nusselt number is found to be a better criterion. Neither of these criteria is free from error. It is well known that convergence toward a particular flow structure may be only a transient, and is followed, sometimes after several diffusion times, by a transition to a new state (Hansen & Ebel 1988; Yuen & Vincent 1988; Christensen 1987). Because of this uncertainty, the *final states* reported here actually correspond to those states that persist long after identifiable transients have vanished. There is no assurance that they would persist indefinitely.

Figure 1 is a regime diagram, summarizing the equilibrium states obtained from the calculations in Table 1. Three distinct flow regimes occur. In order of increasing time variability, these are (1) steady states, (2) pulsating flows, with travelling boundary layer instabilities and fluctuations in cell size and circulation, but with a stationary cell count, and (3) thermally turbulent convection, with non-stationary cell count. Transitions to regimes with stronger time variability occur as either Ra_T or Ra_H increases, but the amount of time dependence is most sensitive to Ra_H.

3.1 Behaviour at low Ra_T

At low thermal Rayleigh numbers, for $Ra_T < 10^5$, internal heat sources increase cell-aspect ratios and induce pulsating time dependence. We have found it useful to describe the time dependence in the pulsating regime in terms of two distinct mechanisms. Time dependence first occurs in the form of weak fluctuations in the circulation within each cell, and slow oscillations in the positions of cell boundaries. We call this the oscillatory subregime. With increased internal heat content, an additional source of time dependence occurs by development of finite-amplitude thermal-boundary-layer instabilities, which travel with the circulation in each cell. We call this the boundary-layer instability regime. This division is somewhat subjective, since in the second subregime, both mechanisms are present simultaneously and both contribute to the time variability.

The change in equilibrium flow structure with increasing Ra_H in the annulus is shown in Figs 2 and 3. Equilibrium cell count decreases with Ra_T (from 10 to 8 between 10^4 and 3.2×10^4), but the change in cell count with Ra_H is even more dramatic. At $Ra_T = 10^4$, the cell count drops from 10 to 6 as Ra_H increases from zero to 4×10^4. At $Ra_T = 3.2 \times 10^4$, the count drops from 8 to 4 as Ra_H increases from zero to 9.6×10^4. Large-aspect ratio cells are evidently the preferred structure for 2-D, low Rayleigh number convection partly driven by internal heat sources. At low Rayleigh numbers, with moderate amounts of internal heat generation present, a steady state can be maintained more easily by large-aspect ratio cellular flow, a structure that allows for a large volume of fluid to reside in the surface thermal boundary layer and thereby lose heat by conduction. Smaller aspect ratio configurations trap more fluid in the core regions of each cell, where heat generation exceeds conductive heat loss, making a steady state more difficult to sustain. Besides the change in cell-aspect ratio,
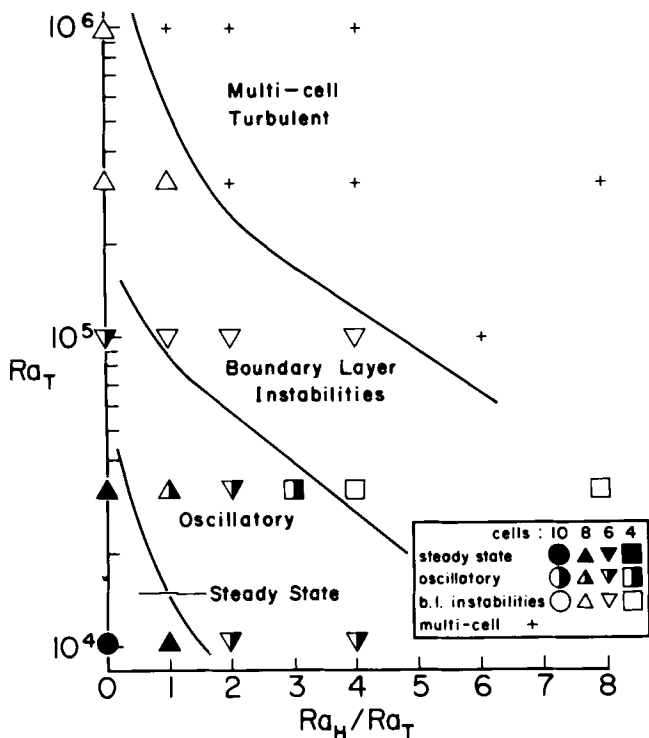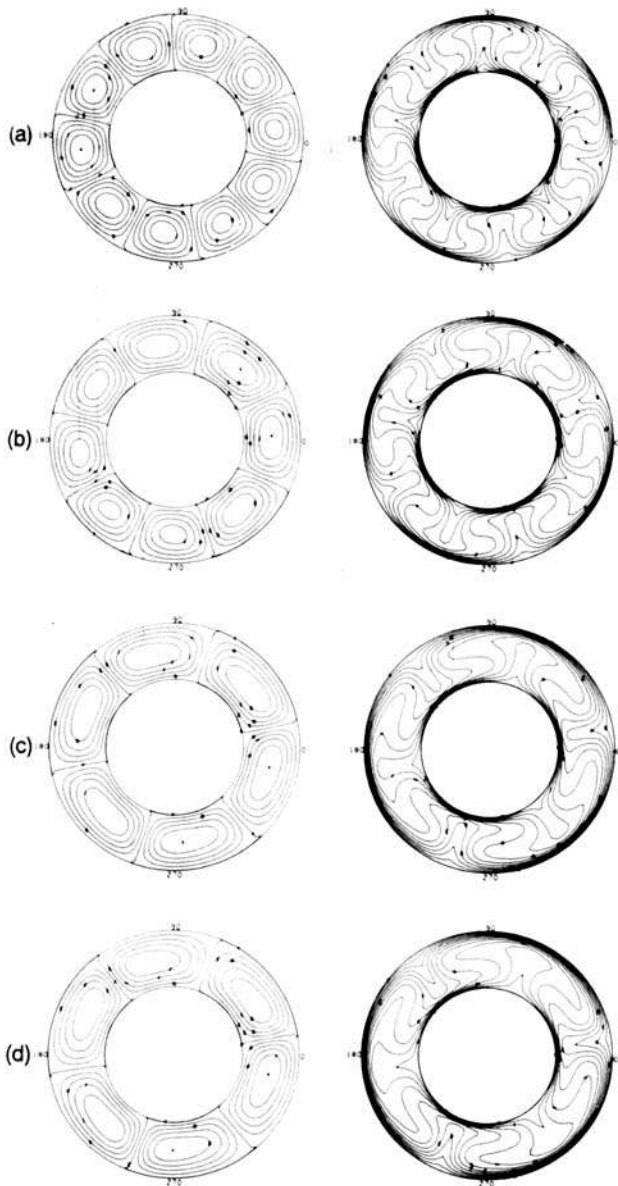

Figure 1. Equilibrium flow regimes for 2-D, infinite Prandtl number thermal convection in the cylindrical annulus. The Rayleigh numbers Ra_T and Ra_H are defined in the text.

Figure 2. Steady-state stream function (left) and temperature (right) contours for $Ra_T = 10^4$ with internal heat generation increasing from top to bottom. Shown are $Ra_H = 0$ (a); 10^4 (b); 2×10^4 (c); 4×10^4 (d).

the main effect of increased heat source content seen in Fig. 2 is an increase in average temperature, or equivalently, the enhancement of the surface thermal boundary layer at the expense of the basal thermal boundary layer. As Ra_H is increased, the buoyancy force becomes increasingly concentrated in the descending plumes, while the ascending plumes become weaker and the ascending flow more diffuse.

Figure 3 shows the change in equilibrium cell aspect ratio at $Ra_T = 3.2 \times 10^4$, for $0 \leq Ra_h \leq 1.28 \times 10^5$. In this case, increased heat-source content not only leads to increased aspect ratio, but precipitates time dependence as well. Steady-state convection in an eight-cell configuration is replaced by time variable, pulsating flow as Ra_H increases from 0 to 1.28×10^5. The weak form of time dependence, slow oscillation of the cell boundaries, can be seen in the
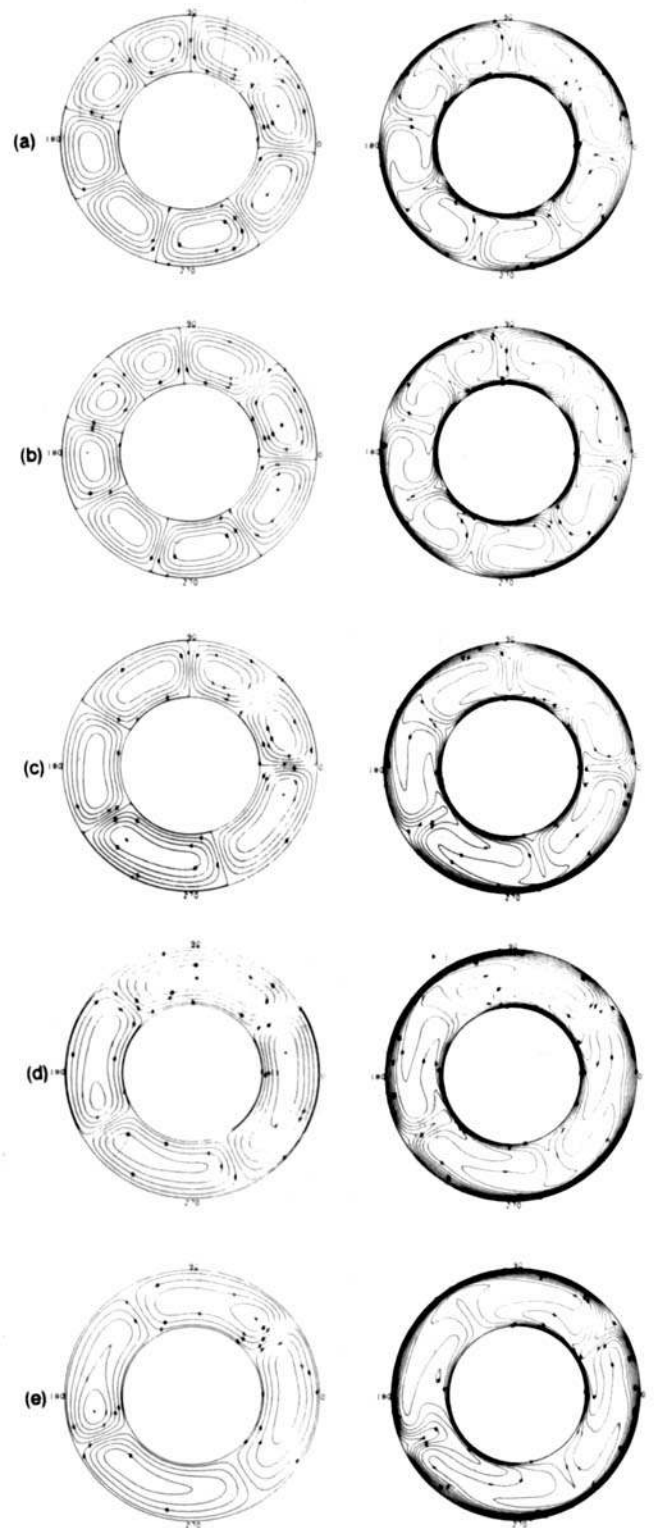
Figure 3. Instantaneous stream function (left) and temperature (right) contours for $Ra_T = 3.2 \times 10^4$ with internal heat generation increasing from top to bottom. Shown are $Ra_H = 0$ (a); 3.2×10^4 (b); 6.4×10^4 (c); 9.6×10^4 (d); 1.28×10^5 (e).

temperature and stream-function fields for $Ra_H = 3.2 \times 10^4$ and 6.4×10^4 (Figs 3b and c). In Fig. 3(c) for example, descending plumes located at 0° and 90° are converging and squeezing the pair of narrow cells between them, while the

pair of long cells across the annulus are extending. The result is a transfer of fluid between adjacent cells. None of the cell cores is closed, and every fluid element must occasionally pass through a cold thermal boundary layer or descending plume. This provides a mechanism for removing the heat generated by volumetric sources from every fluid element of the annulus, and allows a statistical thermal equilibrium to be maintained. If the flow were to settle into a steady state, cell cores would become closed, heat would accumulate within them, and the average temperature of the system would rise, eventually leading to an instability and reorganization of the flow pattern. This scenario is avoided by continual migration of the cell boundaries.

For $Ra_H = 9.6 \times 10^4$ and $Ra_H = 1.28 \times 10^5$, shown in Figs 3(d) and (e), the rate of internal heat production is large enough to force the flow into a four-cell pattern. Time dependence in these cases is due to migrating cell boundaries and to the presence of travelling thermal-boundary-layer instabilities. The direction of movement of cell boundaries can be deduced from the asymmetry of the up- and downwellings. For example, the cell at 90° in Fig. 3(d) and the cells at 0° and at 270° are expanding, while the others are shrinking. In addition, the surface thermal boundary layer contains small-amplitude instabilities, at 0° and 80° in Fig. 3(d) and at 10° and 230° in Fig. 3(e). These perturbations develop by local instability of the thickening thermal boundary layer. They are forced, in part, by temperature heterogeneity in the underlying fluid, as demonstrated by Weinstein *et al.* (1989). They contribute to the variation in average kinetic energy and average Nusselt number by modulating the strength of the descending plumes. As the perturbations are advected out of the thermal boundary layers and into the plumes, they add to the negative buoyancy in the plumes and temporarily accelerate the flow past its average kinetic energy. At times when the plumes are free of perturbations, the kinetic energy is below average.

Figure 4 illustrates the change in cell structure and temperature during the approach to statistical equilibrium, for $Ra_T = 3.2 \times 10^4$ and $Ra_H = 1.28 \times 10^5$. The initial conditions consist of diffusively growing thermal boundary layers, plus the applied random temperature heterogeneity. The initial flow is infinitesimal and is due to the low wavenumber components in the random initial temperature field. In Fig. 4(b), the initial instability of the thermal boundary layers produces a 12-cell pattern. However, this pattern is unstable. It evolves first to an eight-cell pattern, then to six cells and finally to a four-cell pattern (Figs 4c–e). During this evolution, the strength of the surface thermal boundary layer increases at the expense of the basal boundary layer, and the mean temperature of the annulus rises.

The reduction in cell count occurs through mergers of neighbouring descending plumes. This process is illustrated in more detail in Fig. 5, which shows the transition from the six-cell pattern of Fig. 4(d) to the four-cell pattern of Fig. 4(e). The convergence of adjacent descending plumes between 0° and 90° removes fluid from the two small cells located between them. The small cells disappear one at a time, but since the flow is highly unstable with an odd number of cells, as the first small cell vanishes the second one vanishes shortly after.
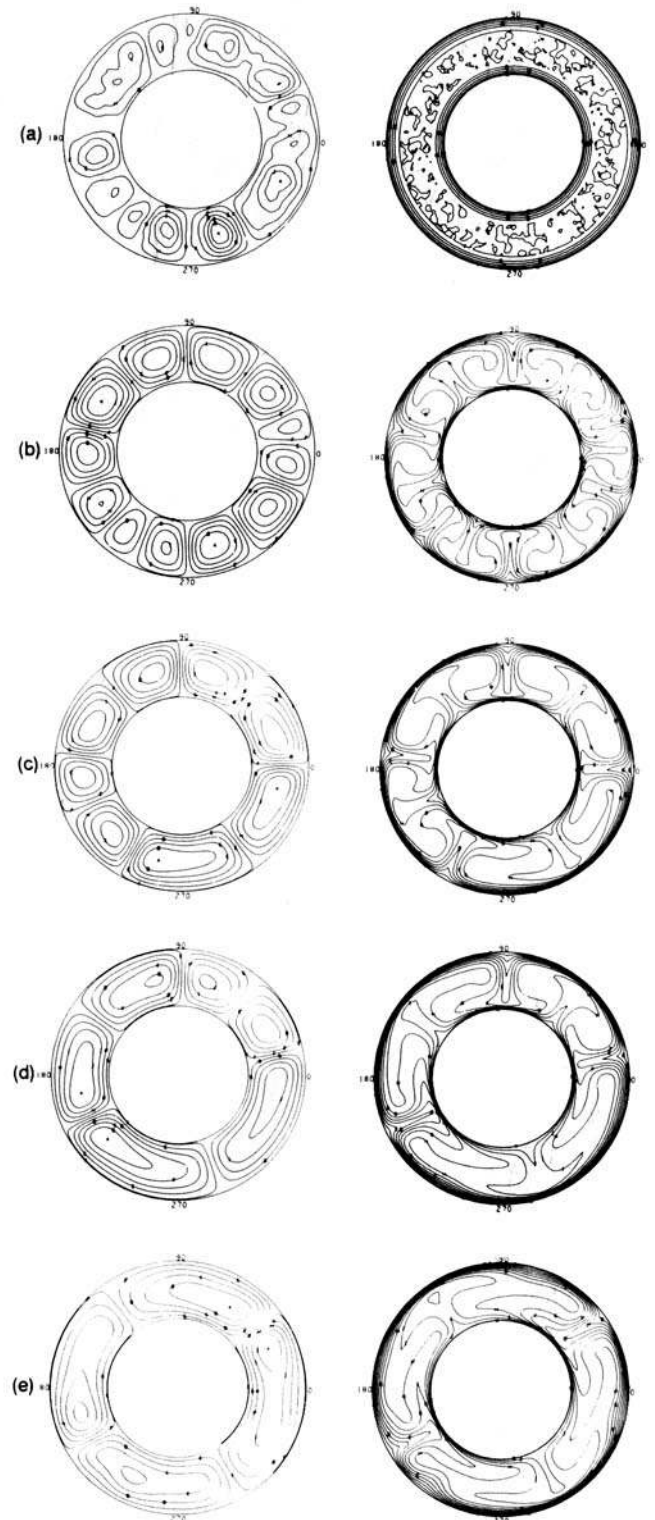
Figure 4. Time evolution of convection at $Ra_T = 3.2 \times 10^4$ and $Ra_H = 1.28 \times 10^5$ starting from random initial temperature conditions. Shown are instantaneous contours of stream function (left) and temperature (right) at dimensionless times $t = 0.0$(a); 0.04(b); 0.15(c), 0.42(d), 1.0(e).

3.2 Convection at higher *Ra* and thermal turbulence

For Rayleigh numbers equal to or in excess of 10^5, both cell migration and boundary-layer instabilities are present, and
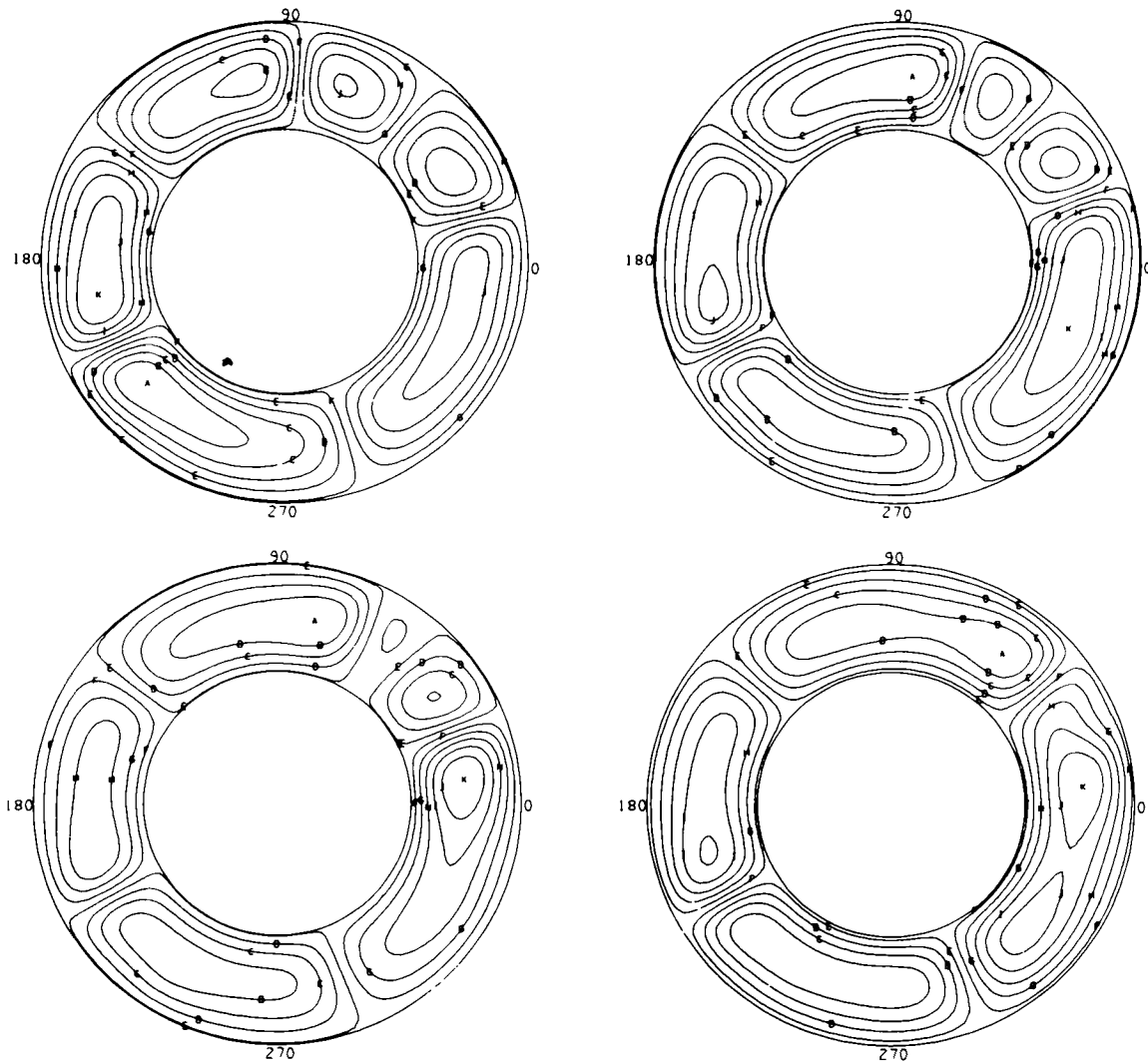
Figure 5. Details of the transition from a six-cell pattern to the equilibrium four-cell pattern at $Ra_T = 3.2 \times 10^4$ and $Ra_H = 1.28 \times 10^5$. Shown are instantaneous stream-function contours starting at $t = 0.5$ in steps of $\delta t = 0.038$.

the convection is always time dependent. In Fig. 6 a comparison is made of the flow pattern and temperature distribution after statistical thermal equilibrium has been reached, for convection with and without internal heat generation, at $Ra_T = 10^5$. In the case of zero internal heat generation (Fig. 6a) the equilibrium flow structure is a six-cell pattern. Travelling instabilities are present in both the surface and the basal thermal boundary layers of the elongated cells, and the positions of the descending and ascending plumes fluctuate with time. However, none of the fluctuations is powerful enough to destroy the six-cell configuration. With the addition of internal heat generation, the strength of the descending plumes increases, the ascending plumes become weaker, and the character of the flow becomes increasingly governed by the dynamics of the surface thermal boundary layer. Fig. 6(b) shows instantaneous stream function and temperature fields after statistical equilibrium has been reached in the case $Ra_H = 6 \times 10^5$. The flow is noticeably more irregular than in the purely base-heated case. In particular, the cell count is no longer invariant with time. New cells are formed as newly formed descending plumes, growing from instabilities

in the surface thermal boundary layer, fall through the interior of pre-existing elongated cells. The start of this process can be seen occuring near 30° in Fig. 6(b). The complementary process, by which cells disappear, occurs through the mergence of converging plumes. The descending plumes located at 90° and 110° are converging and have nearly eliminated the two cells between them. Within a short time the flow in this sector of the annulus will resemble the flow near 225° in Fig. 6(b), where two plumes in close proximity produce a single downwelling. Eventually these pairs merge into a single plume. Repeated formation of new cells by growth of boundary-layer instabilities, and repeated destruction of pre-existing pairs of cells through the mergence of descending plumes, is an additional degree of freedom that occurs for $Ra_T \geq 10^5$ and $Ra_H \geq 0$. We have not found this behaviour in calculations at a lower Rayleigh number, once thermal equilibrium has been reached. We denote the existence of this additional form of time dependence as multi-cell convection or *thermal turbulence*. The adjective *thermal* is used to emphasize the distinction between these flows, in which the Reynolds number is zero and the only non-linearity is heat advection, and turbulent
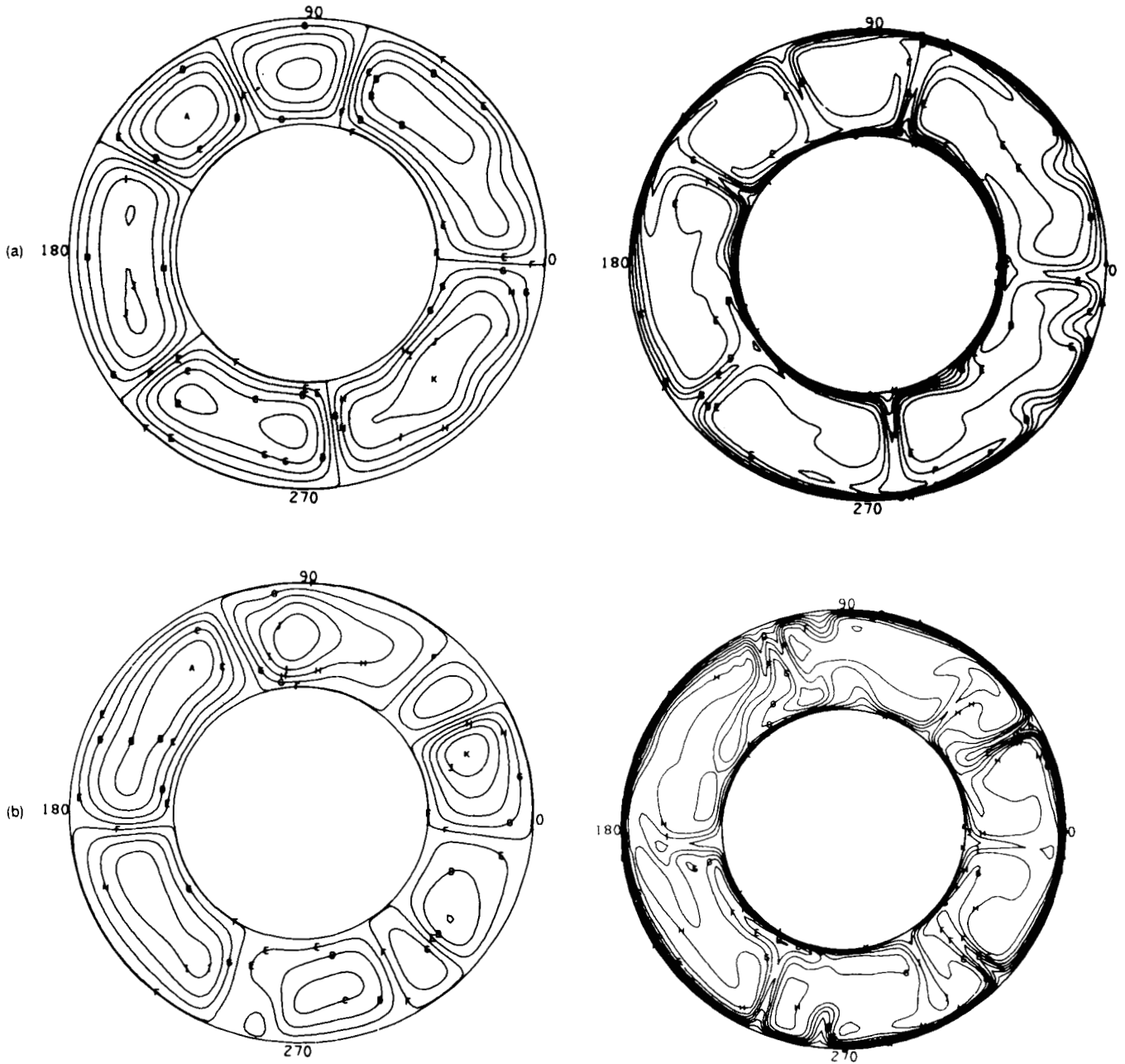
Figure 6. Instantaneous equilibrium stream function (left) and temperature (right) contours for $Ra_T = 10^5$. (a) Six-cell pattern in the boundary-layer instability regime, $Ra_H = 0$; (b) multicellular, thermally turbulent convection at $Ra_H = 6 \times 10^5$.

flow at finite Reynolds number, in which advection of momentum is important.

It is clear from a comparison of Figs 6(a) and (b) that the latter case is not very far into the multicell, thermally turbulent regime. This inference is supported by a comparison of average-kinetic-energy time series and power spectra for the two cases, shown in Figs 7 and 8. The time-averaged kinetic energy is actually larger for the base-heated case. The fluctuations about the time-averaged kinetic energy are indeed somewhat larger in the $Ra_H = 6 \times 10^5$ case, but the difference is rather minor. Kinetic-energy power spectra for these two cases are shown in Figs 8(a) and (b). In the base-heated case, the dominant

frequency is 86.1 cycles per thermal diffusion time, a periodicity of about 3205 Myr. With internal heating the dominant frequency is about 85.1, corresponding to a 3242 Myr periodicity. The spectrum for the base-heated case is dominated by a single line, whereas the spectrum is considerably broader in the mixed heating case. Another property of these calculations is that there are quiet periods in the purely base heated case, when kinetic energy and heat flow seemingly reach steady states, while internal heat generation evidently does not allow this phenomenon to occur. In the case $Ra_T = 10^5$, $Ra_H = 0$, for example, a stationary quiet period persists during the time interval $0.1 \le t \le 0.5$. Quiet periods have been found previously in
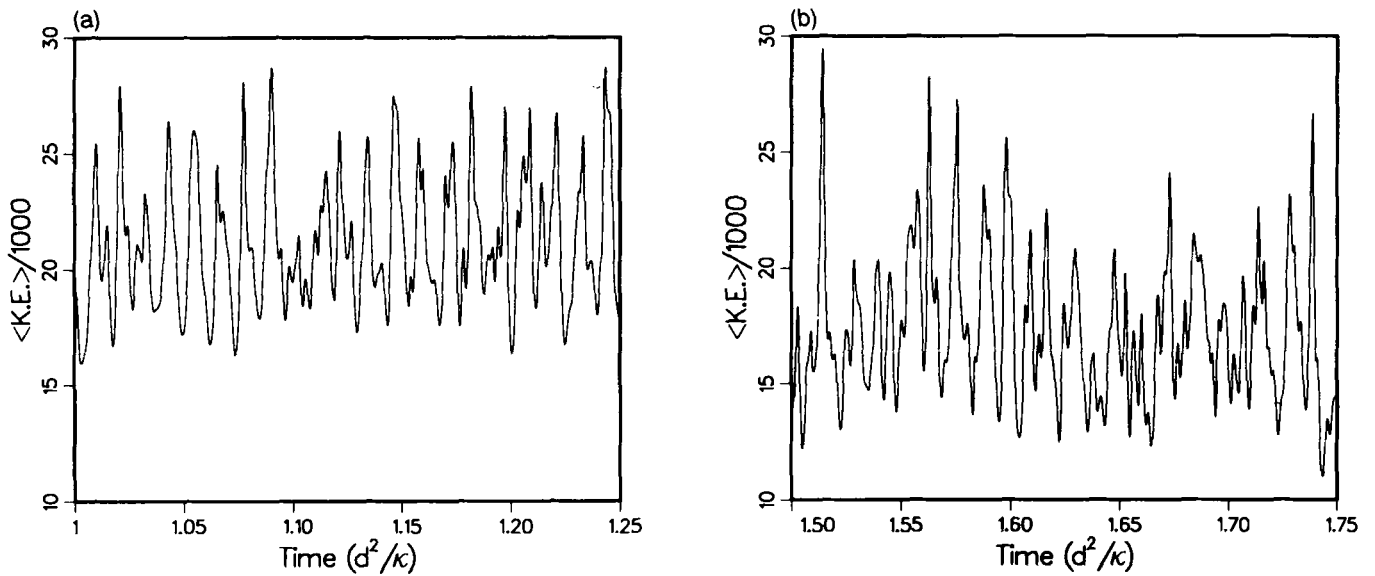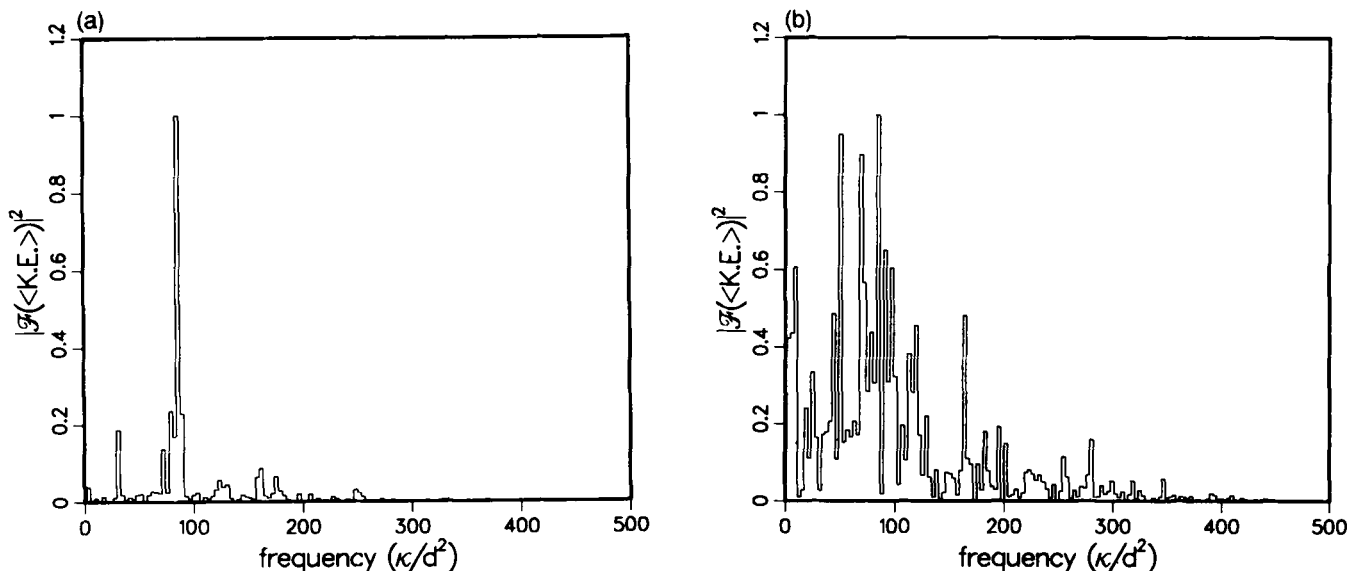
Figure 7. Equilibrium kinetic-energy time series at $Ra_T = 10^5$. (a) $Ra_H = 0$; (b) $Ra_H = 6 \times 10^5$.

time-dependent, base-heated convection calculations (Hansen & Ebel 1988). Another significant point made by results in Figs 7 and 8 is that fully time-dependent, 2-D convection exhibits large fluctuations even in *globally averaged* properties. The total energy of system varies with time at the ±50 per cent level. The fluctuations are not simply local, and do not vanish when averaged over the entire domain.

For $10^5 \le Ra_T \le 10^7$, all calculations with non-zero internal heat production resulted in thermal turbulence. Calculations with zero internal heat production exhibit thermal turbulence above $Ra_T = 10^6$. This is illustrated in Fig. 9, which shows instantaneous stream function and temperature fields in the equilibrium regime at $Ra_T = 10^6$, for $Ra_H = 0$ and 4×10^6. The purely base-heated case (Fig. 9a) exhibits fully developed travelling plume disturbances,

particularly from the surface thermal boundary layer, and an uneven distribution of cell sizes. Despite the presence of vigorous thermal instabilities, we find that the basic eight-cell pattern remains stable, and is able to absorb each starting plume before it can fully disrupt the flow. In contrast, when internal heat generation is present, starting plumes are often strong enough to traverse the entire layer and temporarily subdivide the flow into a greater number of cells, as for example near 90° in Fig. 9(b). The descending plumes are also more mobile in this case because they are less constrained by strong ascending plumes, and the process of cell elimination by plume merger occurs more readily. Infinite Prandtl number thermal turbulence, which we have defined in these calculations as the absence of a stationary cell count, is promoted by internal heat generation. We find

**Figure 8.** Power spectral of kinetic-energy time series from Fig. 7. (a) $Ra_H = 0$; (b) $Ra_H = 6 \times 10^5$.
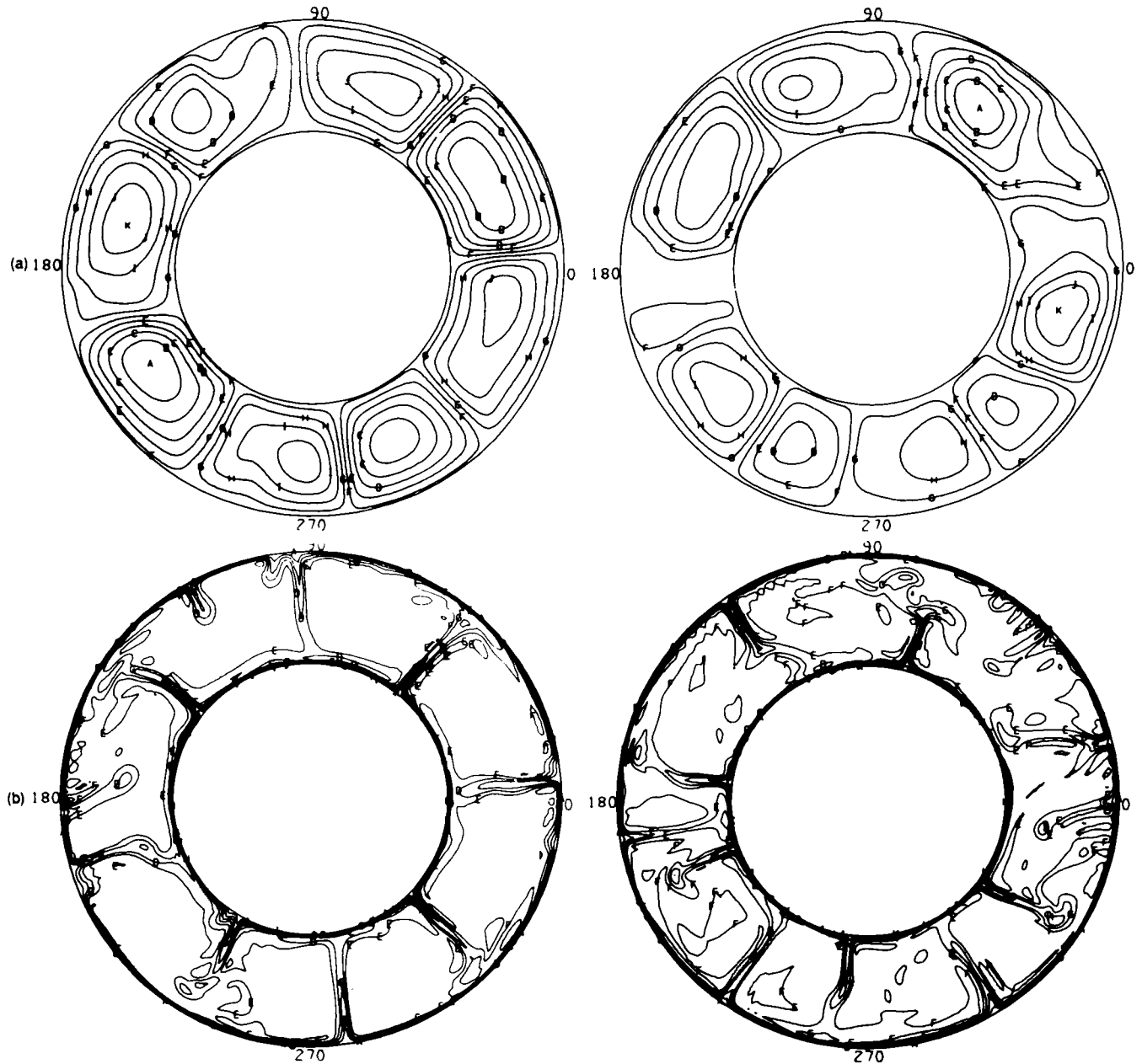
Figure 9. Instantaneous equilibrium stream function (left) and temperature (right) contours for $Ra_T = 10^6$. (a) Eight-cell pattern in the boundary-layer instability regime at $Ra_H = 0$; (b) multicellular, thermally turbulent convection at $Ra_H = 4 \times 10^6$.

that purely base-heated convection also exhibits this behaviour, but at higher Rayleigh numbers. We have limited our study to $Ra_T \le 10^7$ in order to ensure adequate numerical resolution and we observe multicell turbulent convection in purely base-heated calculations only at $Ra_T = 10^7$.

One important characteristic of the multicellular or thermally turbulent regime is that the strength of the circulation varies not only with time, but also with position at a given time. The kinetic-energy density becomes unevenly distributed in azimuth θ with centres of intense circulation alternating with relatively stagnant regions, both of which migrate around the annulus. This behaviour is illustrated by the sequence in Fig. 10, which shows the

instantaneous stream function and temperature fields after thermal equilibrium has been reached, at time intervals of $\delta t = 0.004$, approximately 1000 Myr, for the case $Ra_T = 3.2 \times 10^5$ and $Ra_H = 1.28 \times 10^6$. The cell count fluctuates between 8 and 10, but more importantly, the loci of activity move irregularly around the annulus, and the lifetime of an individual cell is of the order of the transit time of a fluid parcel around a cell. This extreme variability occurs because the circulation is dominated by rapidly growing plumes originating from the surface thermal boundary layer. Pairs of plumes tend to merge soon after a new one develops, which prevents the establishment of a stable cellular pattern. Within the thermally turbulent regime, infinite Prandtl number thermal convection consists of an ensemble of
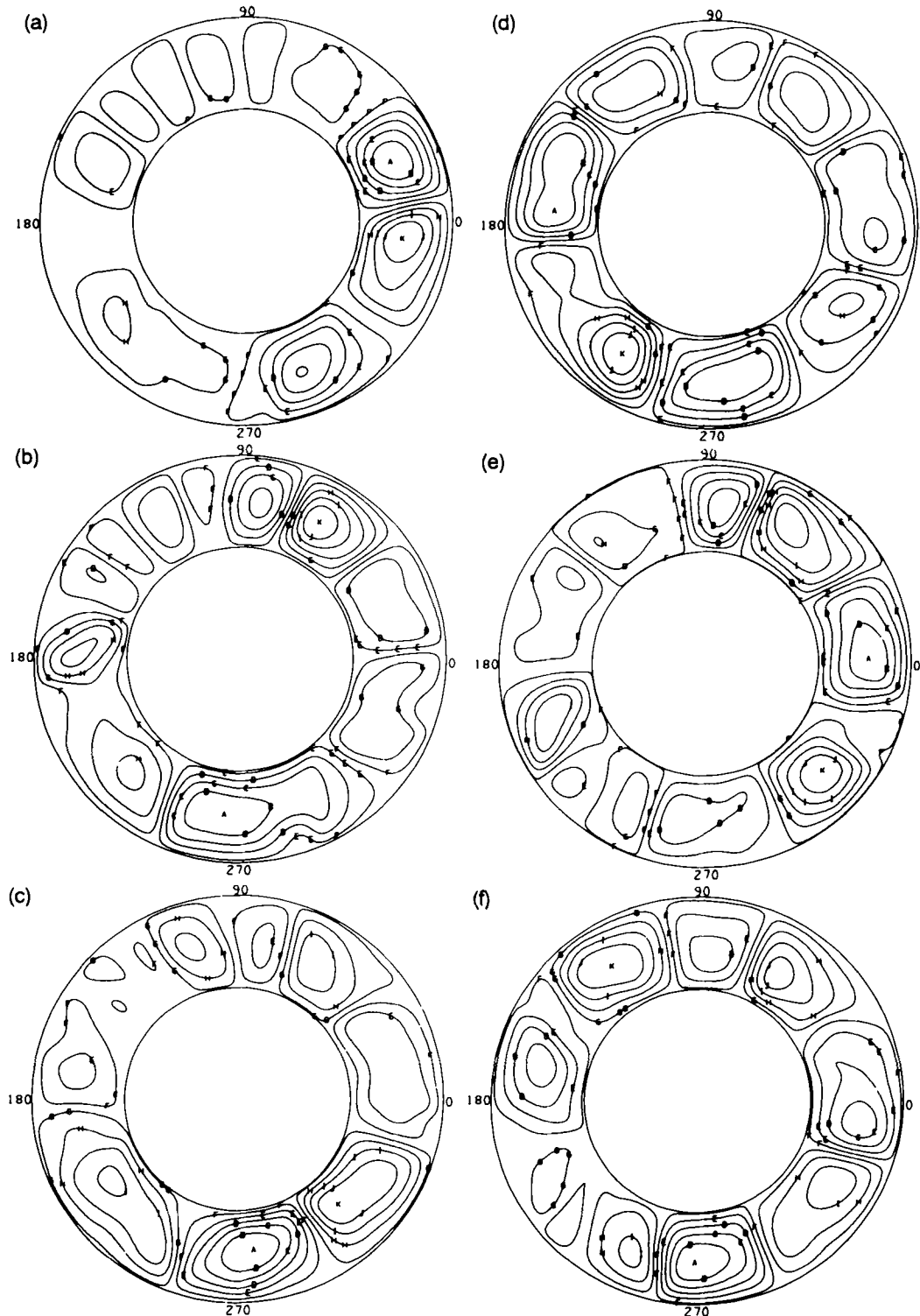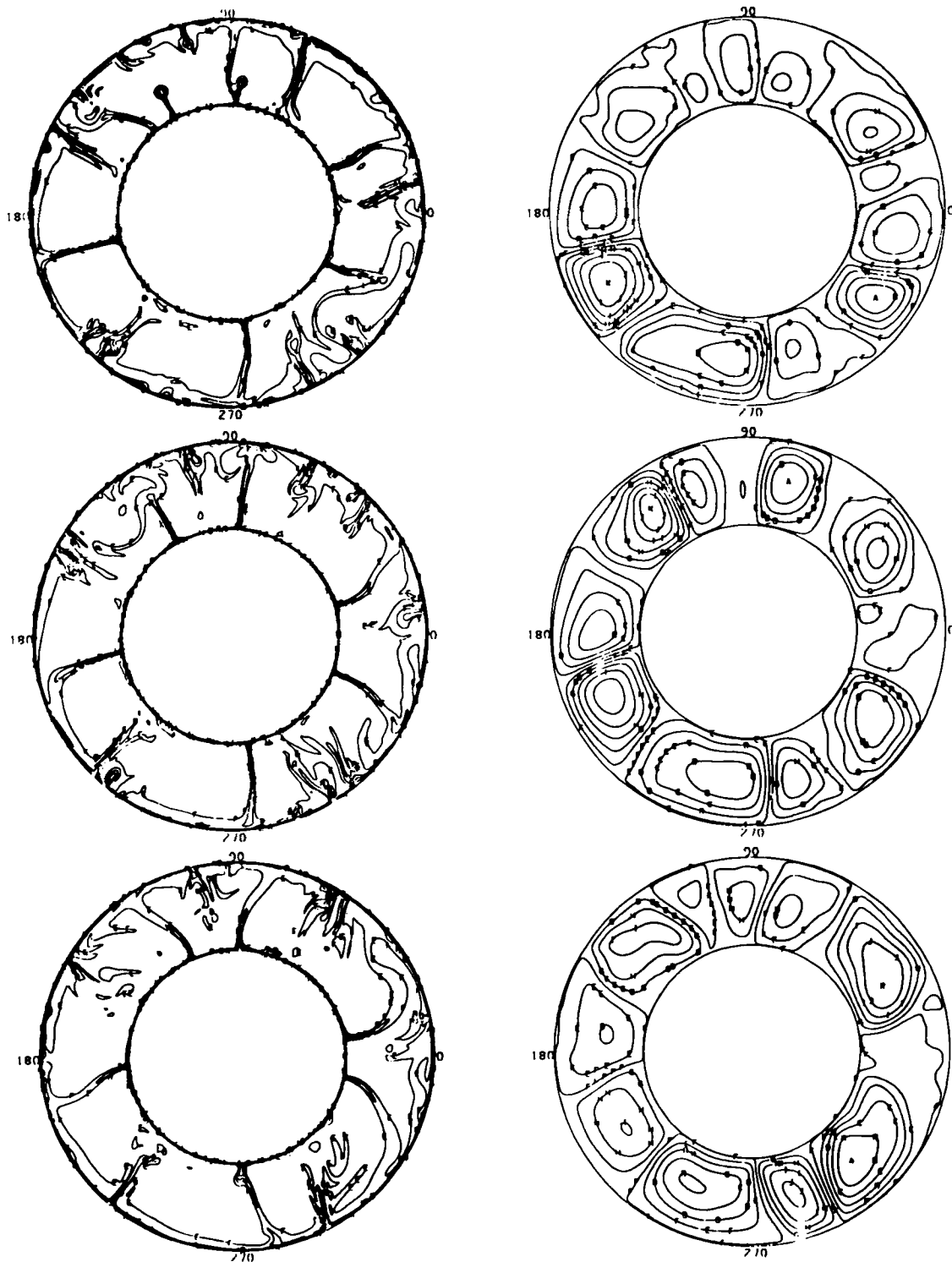
Figure 10. Time evolution of multicellular, thermally turbulent convection at $Ra_T = 3.2 \times 10^5$ and $Ra_H = 1.28 \times 10^6$. Shown are instantaneous contours of stream function at dimensionless time intervals $\delta t = 0.004$, approximately 10^9 yr.

transient episodes of plume formation, superimposed on an ensemble of equally frequent plume mergers.

Three calculations at $Ra_T = 10^7$ have been made, one purely base heated ($Ra_H = 0$), the other two with $Ra_H = 6 \times 10^7$ and $Ra_H = 24 \times 10^7$ respectively. At these Rayleigh numbers, all cases with internal heat generation are characterized by vigorous thermally turbulent convec-

tion. Narrow, transient plumes separate from both thermal boundary layers and traverse the annulus, continually reorganizing the pattern of motion. Plumes often collide and deflect other plumes originating from the opposite boundary layer. Plume widths are typically 1/30 times the annulus depth, equivalent to about 100 km in the mantle. Initiation of new plumes is not everywhere synchronous in time, and
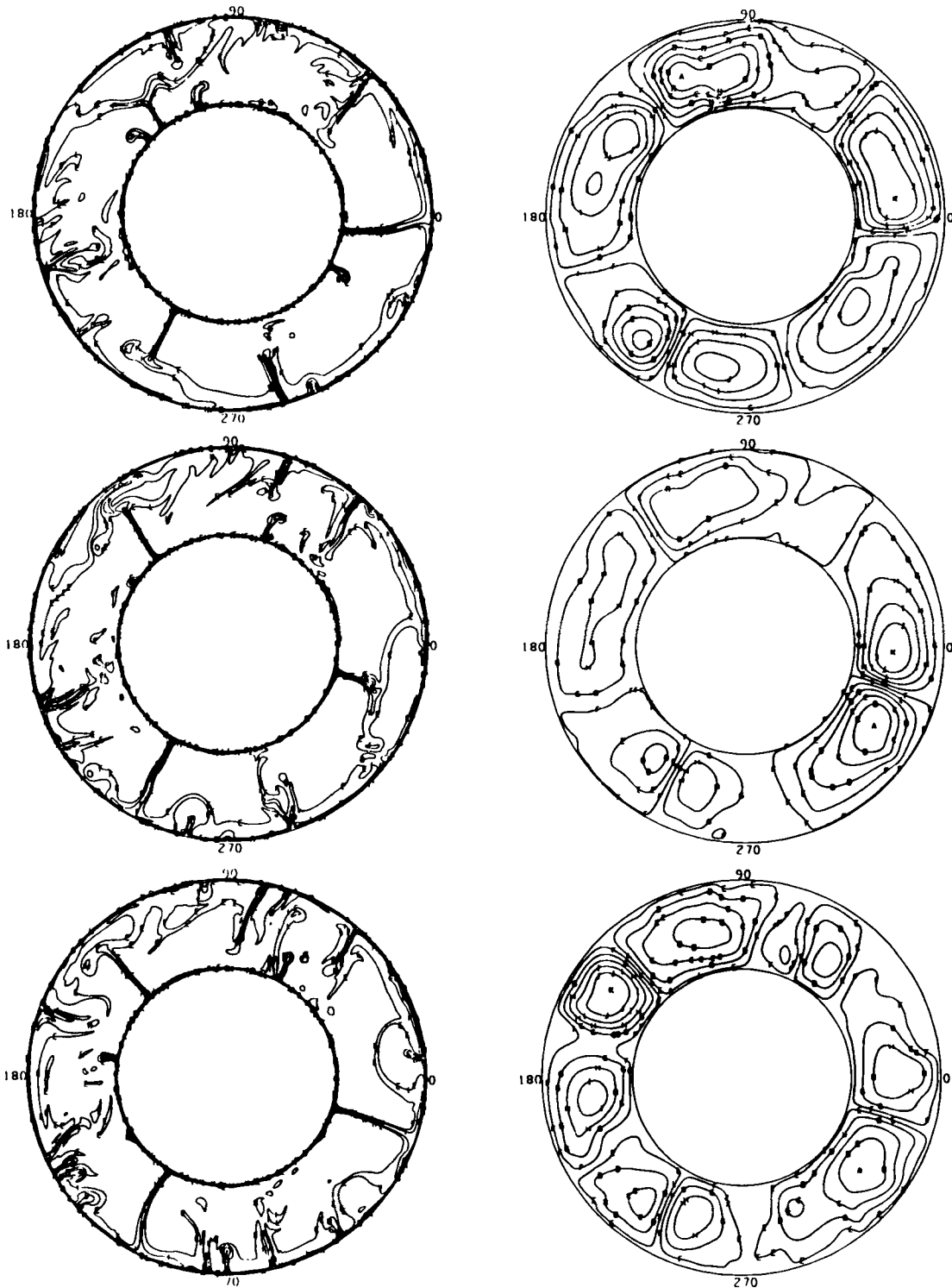
Figure 11. Time evolution of multicellular, thermally turbulent convection at $Ra_T = 10^7$ and $Ra_H = 0$. Shown are instantaneous contours of stream function and temperature at dimensionless time intervals $\delta t = 0.0002$, approximately 50 Myr.

the sites of new plume formation are irregularly distributed around the annulus. For the cases with internal heat production, this behaviour results in continual variation in the number of cells.

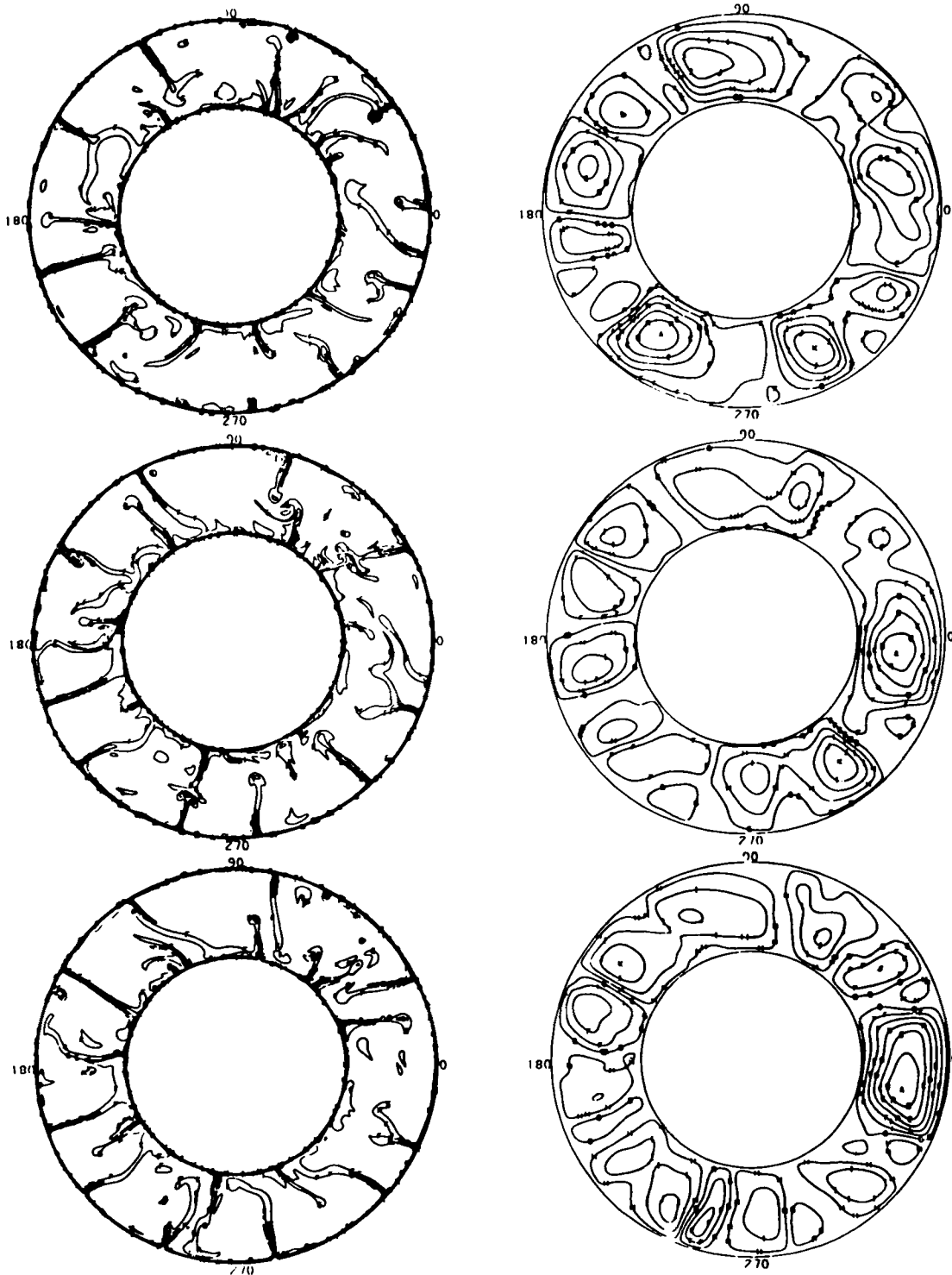Figure 11 shows temperature and stream-function contours for the base-heated case at 50 Myr time intervals.

Variability in the cell count is only just evident on this time-scale. This case is apparently near the boundary between turbulent and non-turbulent convection. The intensity of convection is not uniform around the annulus. Relatively quiet regions alternate with active regions, and the distribution of activity changes with time. At this

Figure 12. Time evolution of multicellular, thermally turbulent convection at $Ra_T = 10^7$ and $Ra_H = 6 \times 10^7$. Shown are instantaneous contours of stream function and temperature at dimensionless time intervals $\delta t = 0.0002$, approximately 50 Myr.

Rayleigh number, the average fluid velocity varies between 2–4 cm yr^{-1}. Although instabilities develop at seemingly random places around the core–mantle boundary, they tend to move toward one of several fairly stationary separation points before growing into large plumes. These separation points, located at approximately 90, 190 and 350° in Fig. 14,

are quite persistent, but the number of instabilities that collect in each locality varies considerably in time. Downwellings are not as concentrated as upwellings in this calculation, and behave more passively. The downwellings are composed of the tips of rising plumes that have spread out across the upper surface. Thermal anomalies associated

Figure 13. Time evolution of multicellular, thermally turbulent convection at $Ra_T = 10^7$ and $Ra_H = 24 \times 10^7$. Shown are instantaneous contours of temperature (left column) and stream function (right column) at dimensionless time intervals $\delta t = 0.0002$, approximately 50 Myr.

with the sinking plumes are generally restricted to the upper half of the annulus, rather than being continuous across the entire depth.

Figure 12 shows temperature and stream-function contours with internal heat generation at $Ra_T = 10^7$ and $Ra_H = 6 \times 10^7$, at time intervals of approximately 50 Myr. In this

calculation the cell count is more variable than in the purely base-heated case, although three persistent separation points are evident near 120°, 240° and 350°. The thermal-boundary-layer instabilities converge toward these points, although occasionally some develop and rise through the annulus before reaching the major upwellings. The

sinking plumes are more energetic in this case, compared with the purely base-heated calculation, but nevertheless are not as energetic as the upwellings. The descending plumes are typically composite structures, composed of three strands, the central plume and two flanking plumes derived from instabilities swept in from the heads of adjacent plume heads.

Figure 13 shows temperature and stream-function contours with internal heat generation at $Ra_T = 10^7$ and $Ra_H = 24 \times 10^7$, at 50 Myr time intervals. In this case the cells are highly irregular and vary in intensity and size on this time-scale. Sinking plumes are the preferred mode of instability with this amount of internal heat generation. Some rising plumes are in evidence, but they appear to be driven as much by the convergence between adjacent downwelling regions as by hot boundary-layer instabilities. Collisions between rising and sinking plumes are seen, for example near 250° in Fig. 13(b). At any instant in time, the thermal anomalies associated with rising or sinking plumes are not continuous across the annulus. In thermally turbulent convection, the transience of the flow inhibits the radial continuity of plume structures seen at lower Rayleigh numbers. In effect the upper and lower thermal boundary layers act as partially decoupled sources of convection, and the flow is less organized and more chaotic as a consequence. The transience and extreme narrowness of the thermal plumes in these simulations has important implications for attempts to model mantle convection in three dimensions. At realistic mantle Rayleigh numbers of the order $Ra_T = 10^7$, grid spacing of 50–100 km in all three dimensions is needed to resolve the thermal structures produced in these calculations. Too coarse a resolution has the effect of lowering the effective Rayleigh number, resulting in a completely different flow regime in the calculation.

For the calculations in Figs 11–13, the time-averaged surface heat flow during the final 10^9 years are 48, 53 and 66 mW m^{-2}, respectively. The last value, obtained from the $Ra_H = 24 \times 10^7$ calculation, is representative of the average geothermal flux, with the contribution from radioactivity in the continental crust removed. In this calculation, basal heating accounts for approximately 40 per cent of the total surface heat flow. In the Earth, it is estimated that about 20 per cent of mantle heat flow is derived from the core, so that this calculation represents an extreme upper bound to the amount of basal heating. Increasing the proportion of internal to basal heating would enhance thermal turbulence still further.

One measure of the time variability in these flows is the rate at which stagnation points form, migrate, and disappear on the upper surface. This visualization technique has been used recently by D. Yuen and co-workers, as a means of depicting the level of time variability in convection, and determining the transition to thermal turbulence (see Hansen *et al.* 1990, for an example). Figs 14(a) and (b) show traces of the stagnation points versus time at $Ra_T = 10^7$ for the $Ra_H = 0$ and $Ra_H = 24 \times 10^7$ cases, respectively. The traces are the locus of points on the surface where the horizontal velocity changes sign. It is clear from the slow migration of the traces in Fig. 14(a) that the cells in the purely base-heated case are persistent and the convection is not strongly turbulent. Typically, the stagnation points drift
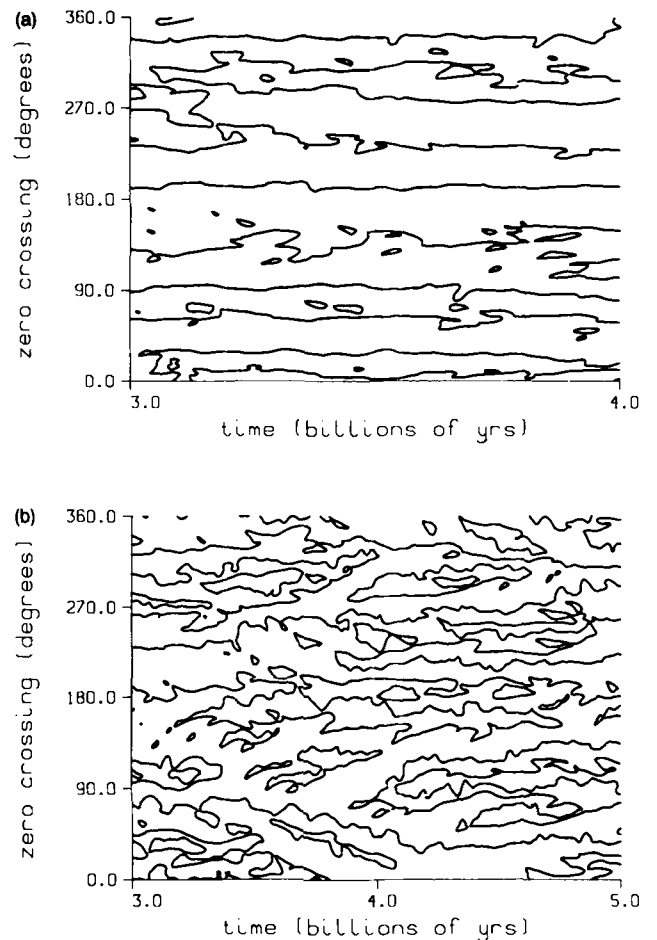
Figure 14. Positions of cell boundaries versus time on the upper surface of the annulus. Top: $Ra_T = 10^7$ $Ra_H = 0$ Bottom: $Ra_T = 10^7$ $Ra_H = 24 \times 10^7$.

less than 20° in 4000 Myr, and there are only brief and relatively minor changes in cell count. In contrast, the $Ra_H = 24 \times 10^7$ case is much more variable. In this calculation, the cell count changes on 500 Myr time-scales, and the rate of boundary migration is much more rapid. The presence of internal heat generation clearly increases the level of turbulence.

3.3 Episodicity

In addition to local fluctuations, thermally turbulent convection exhibits fluctuations in global quantities, such as total heat transport and total kinetic energy. The kinetic-energy profiles shown in Fig. 15 for the $Ra_T = 10^7$ calculations contain episodes of relative quiet and relative activity, with widely variable durations. The largest fluctuations in kinetic energy are of the same order as the time-averaged kinetic energy, and there are numerous fluctuations of 20–30 per cent of the time-averaged value. These fluctuations are caused by variations in the strength and number of descending and ascending thermal plumes, which in turn cause variations in the number and size of thermal-boundary-layer instabilities.

Also shown in Fig. 15 are the power spectra of kinetic energy for the three calculations. These were computed
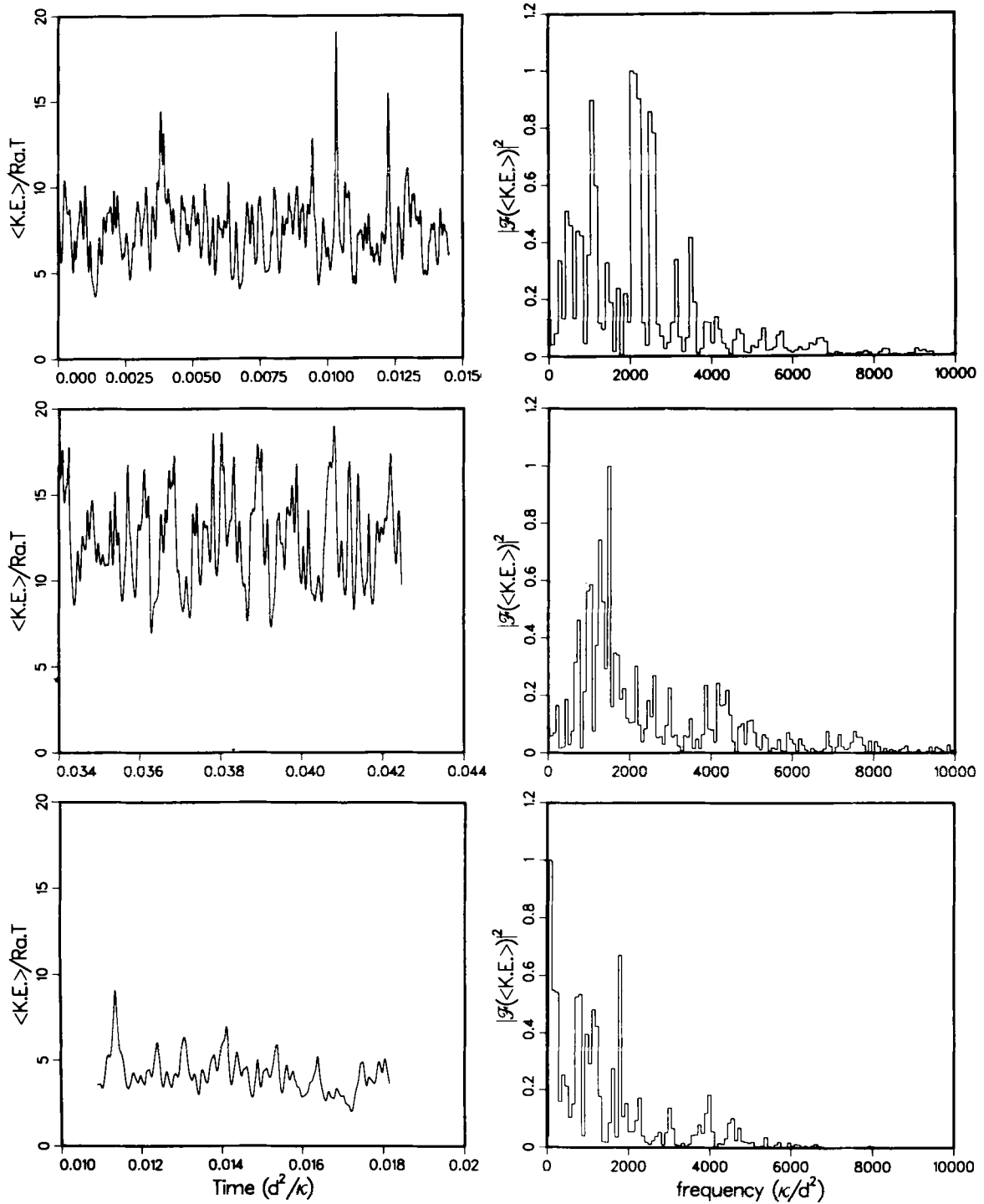
Figure 15. Kinetic-energy time series (left column) and corresponding power spectra (right column) at $Ra_T = 10^7$. Top: $Ra_H = 0$; middle: $Ra_H = 6 \times 10^7$; bottom: $Ra_H = 24 \times 10^7$.

using only the final several Ga of each calculation, after statistical thermal equilibration had been reached. Tables 2, 3 and 4 list the periods of the main spectral peaks in Myr, calculated assuming a thermal diffusivity of $10^{-6}\,\mathrm{m^2\,s^{-1}}$. In the purely base-heated case, the peak power corresponds to a periodicity of about 134 Myr, with additional power at shorter periods, including 110 Myr, 80–90 Myr and 60–70 Myr. For the calculation with $Ra_H = 6 \times 10^7$, the largest

peak is near 186 Myr. As in the base heated case, there is also considerable power at longer periods, as well as shorter ones, in the 90–120 Myr and 65–70 Myr ranges, for example. In the $Ra_H = 24 \times 10^7$ calculation, the peak power is at a very long time-scale, 3500 Myr, representing the secular evolution. Significant secondary peaks occur at 350 and 150 Myr, and energy is also concentrated in the 90–120 and 60–70 Myr ranges.

Table 2. Kinetic-energy spectral peaks at $Ra_T = 10^7$, $Ra_H = 0$.

Dimensionless Frequency	Relative Power	Period (Myr)
448	0.511	615
717	0.441	385
1076	0.897	256
1434	0.329	192
1703	0.238	162
2062	1.0	134
2510	0.856	110
3137	0.339	88
3496	0.416	79
3855	0.121	72
4123	0.138	67

Table 3. Kinetic-energy spectral peaks at $Ra_T = 10^7$, $Ra_H = 6 \times 10^7$.

Dimensionless Frequency	Relative Power	Period (Myr)
708	0.524	389
1030	0.645	268
1223	0.628	225
1481	1.0	186
1803	0.282	153
2124	0.272	130
2640	0.209	104
3026	0.239	91
3476	0.136	79
3863	0.345	71
4249	0.285	65
5022	0.148	55

Table 4. Kinetic-energy spectral peaks at $Ra_T = 10^7$, $Ra_H = 24 \times 10^7$.

Dimensionless Frequency	Relative Power	Period (Myr)
78.7	1.0	3505
472	0.295	584
787	0.752	350
1181	0.465	234
1811	0.667	152
2283	0.181	121
2992	0.129	92
4015	0.173	69
4566	0.102	60

4 CONSEQUENCES OF THERMAL TURBULENCE IN THE MANTLE

It is an obvious fact that convection in the Earth's mantle is unsteady. The unsteadiness occurs on a spectrum of time-scales, ranging from the age of the Earth down to a million years and perhaps shorter. The longest time-scales, the secular evolution, are in response to irreversible processes such as the declining abundance of heat producing elements, and chemical fractionation due to partial melting. These forms of time dependence are usually referred to as *thermal history*. The preferred model for thermal history is

one in which the earth cools by 40–80 K Gyr^{-1} (Davies 1980; Schubert, Stevenson & Cassen 1980), and the vigour of convection decreases largely because of an increase in average viscosity. The secular evolution style of time dependence need not involve any change in the *structure* of mantle convection. Indeed, the simple models of thermal history implicitly assume the structure of mantle convection is time invariant, and only the amplitude of the motion changes with time. The other expression of time dependence, the one considered in this paper, is *intrinsic* to thermal convection at large Rayleigh numbers. It is a result of the non-linear dynamics of mantle convection, and involves continuous changes in the *structure*, as well as changes in the amplitude of the motion.

The structure of convection in the mantle is necessarily time dependent, as indicated by the irregular geometry of convergent and divergent plate boundaries and the absence of a perfect balance between the rates of sea-floor creation and subduction for individual plates. (Forsyth & Uyeda 1975; Solomon & Sleep 1974, Kaula 1975; Chase 1978; Minster & Jordan 1978, Parsons 1981). Mantle convection therefore cannot consist of steady flow in closed cells. The instantaneous positions of cell boundaries must drift through the mantle, in order for mass transfer to occur beneath neighbouring plates. It has been established, for example, that most if not all trenches (and by inference, the slabs as well) migrate through the mantle with a retrograde transverse velocity that is comparable to the down-dip, longitudinal velocity that is often used to characterize subduction (Chase 1978; Garfunkel, Schubert & Anderson 1986). This motion requires a reduction in area of the subducting plate with time, and a corresponding reduction in the size of the circulation beneath the plate. There are several identifiable causes for the continual reorganization of plate geometry. The presence of continents, which represent lithospheric heterogeneity in rheological and thermal properties, plays an important role (Gurnis 1988). Another cause is the rheology of oceanic plates, which permits only one plate to be subducted at a convergent boundary, insuring mass transfer beneath adjacent plates at subduction zones.

In addition to local variability, the globally averaged intensity of mantle convection also fluctuates with time. We infer this from fluctuations in the global rate of sea-floor spreading, subduction and hotspot volcanism. For example, the subduction rate, the sea-floor spreading rate and hotspot activity were all higher during the Cretaceous than before and since (Larson 1991; Larson & Olson 1991; Richards & Engebretson 1992). This non-monotonic variability is not predicted by parametrized thermal-history models. However, fluctuations in global tectonic and volcanic activity are easily explained in terms of the dynamics of mantle convection. Calculations such as those presented here demonstrate that high Rayleigh number thermal convection exhibits pulses of high globally averaged kinetic energy, which offers an explanation for the episodic character of the geologic record. Our calculations demonstrate that time dependence in convection is due in part to the presence of secondary flows driven by thermal plumes that develop from instabilities in both of the thermal boundary layers. At a Rayleigh number of 10^7, the fluid velocities are typically 1–6 cm yr^{-1}, within the range of plate speeds, and the

thermal boundary layers are typically 50–100 km thick, similar to the thermal thickness of oceanic lithosphere. This is also the regime of fully developed thermal turbulence in the calculations. In the thermally turbulent regime, the boundary layers behave almost independently of each other. All of the thermal plumes are transient structures, and the flow pattern is reorganized on the overturn time-scale, which is a few hundred million years. The distribution of cold plumes descending from the top boundary layer is not closely coupled to the distribution of hot plumes ascending from the basal boundary layer, and many of the cold and hot structures are not continuous across the entire depth of the annulus. In the thermally turbulent regime, the sizes of the individual cells present at any instant in time are highly variable, and the strength of the circulation, as measured by the total kinetic energy, varies with position around the annulus and with time. These characteristics are not found at lower Rayleigh numbers where thermal turbulence is absent. It suggests that a possible explanation for the large differences in plate sizes and sea-floor spreading rates found in present-day tectonics can be found by appealing to this style of convection. The kinetic-energy spectra show periodicities ranging from 400 to 40 Myr. These are similar in length to the basic divisions of Earth history that define the geologic time, and suggests that geologic time may be governed by the variability in mantle convection.

The characteristics of time-dependent thermal convection in these calculations are certainly not identical with the character of time variability in mantle convection. The system we have analysed here is far too idealized to be a close analogue to the mantle. We have deliberately ignored the effects of phase transitions, for example. But the correspondence between time-dependent behaviour in the model and what is known of the time-dependent behaviour of the mantle suggests a similarity in the underlying physical cause. Mantle convection is characterized by high Rayleigh numbers and the presence of large amounts of internal heat generation. Given these conditions, time-dependent convection is *inevitable* and thermal turbulence is possible.

ACKNOWLEDGMENTS

REFERENCES

Bercovici, D., Schubert, G. & Glatzmaier, G.A., 1989. Influence of heating mode on three-dimensional mantle convection, *Geophys. Res. Lett.*, **16**, 617–629.

Castaing, B., Gunarantne, G., Heslot, F., Kadanoff, L., Libchaber, A., Thomae, S., Wu, X.Y., Zaleski, S. & Zanetti, B., 1989. Scaling of hard thermal turbulence in Rayleigh–Benard convection, *J. Fluid Mech.*, **204**, 1–30.

Chase, C.G., 1978. Plate kinematics: The Americas, East Africa and the rest of the world, *Earth planet. Sci. Lett.*, **37**, 355–368.

Christensen, U., 1987. Time-dependent convection in elongated Rayleigh–Benard cells, *Geophys. Res. Lett.*, **14**, 220–223.

Christensen, U. & Yuen, D.A., 1989. Time-dependent convection with non-Newtonian viscosity, *J. geophys. Res.*, **94**, 814–820.

Davies, G.F., 1980. Thermal histories of convective earth models and constraints on radiogenic heat production in the Earth, *J. geophys. Res.*, **85**, 2517–2530.

Davies, G.F., 1988. Role of the lithosphere in mantle convection, *J. geophys. Res.*, **93**, 10 451–10 466.

Forsyth, D.W. & Uyeda, S., 1975. On the relative importance of the driving forces of plate tectonics, *Geophys. J.R. astr. Soc.*, **43**, 163–200.

Garfunkel, Z., Schubert, G. & Anderson, C.A., 1986. Mantle circulation and the lateral migration of subducted slabs, *J. geophys. Res.*, **91**, 7205–7223.

Gurnis, M., 1988. Large-scale mantle convection and the aggregation and dispersal of supercontinents, *Nature*, **332**, 695–699.

Gurnis, M. & Zhong, S., 1991. Generation of long wavelength heterogeneity in the mantle by the dynamic interaction between plates and convection, *Geophys. Res. Lett.*, **18**, 581–584.

Hansen, U. & Ebel, A., 1988. Time-dependent thermal convection: a possible explanation for a multi-scale flow in the Earth's mantle, *Geophys. J.*, **94**, 181–194.

Hansen, U., Yuen, D.A. & Kroening, S.E., 1990. Transition to hard turbulence in thermal convection at infinite Prandtl number, *Phys. Fluids A*, **2**, 2157–2163.

Houseman, G., 1988. The dependence of convective planform on mode of heating, *Nature*, **332**, 346–349.

Jarvis, G.T., 1984. Time-dependent convection in the Earth's mantle, *Phys. Earth planet. Inter.*, **36**, 305–327.

Kaula, W.M., 1975. Absolute plate motions by boundary velocity minimizations, *J. geophys. Res.*, **80**, 244–248.

Krishnamurti, R., 1970. On the transition to turbulent convection, *J. Fluid Mech.*, **42**, 295–320.

Larson, R., 1991. Latest pulse of the Earth: evidence for a mid-Cretaceous superplume, *Geology*, **19**, 547–550.

Larson, R. & Olson, P., 1991. Mantle plumes control magnetic reversal frequency, *Earth planet Sci. Lett.*, **107**, 437–447.

Machetel, P. & Weber, P., 1991. Intermittent layered convection in a model with an endothermic phase change at 670 km, *Nature*, **350**, 55–57.

Machetel, P. & Yuen, D.A., 1987. Chaotic axisymmetrical spherical convection and large-scale mantle circulation, *Earth planet. Sci. Lett.*, **86**, 93–104.

Machetel, P. & Yuen, D.A., 1989. Penetrative convective flows induced by internal heating and mantle compressibility, *J. geophys. Res.*, **94**, 10 606–10 626.

Malevsky, A.V. & Yuen, D.A., 1992. Strongly chaotic non-Newtonian mantle convection, *Geophys. astrophys. Fluid Dyn.*, **65**, 149–171.

McKenzie, D.P., Roberts, J.M. & Weiss, N.O., 1974. Convection in the Earth's mantle: towards a numerical simulation, *J. Fluid Mech.*, **62**, 465–538.

Minster, J.B. & Jordan, T.H., 1978. Present-day plate motions, *J. geophys. Res.*, **83**, 5331–5354.

Olson, P., 1987. A comparison of heat transfer laws for mantle convection at very high Rayleigh numbers, *Phys. Earth planet. Inter.*, **48**, 153–160.

Parsons, B., 1981. The rates of plate creation and consumption, *Geophys. J.R. astr. Soc.*, **67**, 437–448.

Peltier, W.R. & Solheim, L.P., 1992. Mantle phase transitions and layered chaotic convection, *Geophys. Res. Lett.*, **19**, 321–324.

Ramshaw, J. & Dukowicz, J., 1979. APACHE: a generalized-mesh Eulerian computer code for multicomponent chemically reactive fluid flow, *Los Alamos National Lab. Rep LA*-7427.

Richards, M.A. & Engebretson, D.C., 1992. The history of subduction and large scale mantle convection, *Nature*, **355**, 437–440.

Schubert, G. & Anderson, C.A., 1985. Finite element calculations of very high Rayleigh number thermal convection, *Geophys. J.R. astr. Soc.*, **80**, 575–601.

Schubert, G., Stevenson, D. & Cassen, P., 1980. Whole planet cooling and radiogenic heat source contents of the earth and moon, *J. geophys. Res.*, **85**, 2531–2538.

Solheim, L. & Peltier, W.R., 1990. Heat transfer and the onset of chaos in a spherical, axisymmetric anelastic model of whole mantle convection, *Geophys. astrophys. Fluid Dyn.*, **53**, 205–255.

Solomon, T.H. & Gollub, J.B., 1991. Thermal boundary layers and heat flux in turbulent convection: the role of recirculating flows, *Phys. Rev.* A, **43**, 6683–6693.

Solomon, S.C. & Sleep, N.H., 1974. Some simple physical models for absolute plate motions, *J. geophys. Res.*, **79**, 2557–2567.

Swarztrauber, P. & Sweet, R., 1975. Efficient Fortran subprogram for the solution of elliptic equations, NCAR TNIA-109.

Tackley, P.J., Stevenson, D.J., Glatzmaier, G.A. & Schubert, G., 1993. Effects of an endothermic phase transition at 670 km depth in a spherical model of convection in the Earth's mantle, *Nature*, **361**, 699–704.

Travis, B., 1990. Numerical models of 2-D and 3-D geophysical convection, in *Heat Transfer in Earth Science Studies*, ASME series, 149, eds Carrigan, C. & Chu, T.Y.

Travis, B., Olson, P. & Schubert, G., 1990. The transition from two-dimensional to three-dimensional planforms in infinite Prandtl number thermal convection, *J. Fluid Mech.*, **216**, 71–91.

Travis, B., Weinstein, S. & Olson, P., 1990. Three-dimensional planforms with internal heat generation, *Geophys. Res. Lett.*, **17**, 243–246.

Vincent, A. & Yuen, D.A., 1988. Thermal attractor in chaotic convection wth high Prandtl number fluids, *Phys. Rev.*, **A38**, 328–334.

Weinstein, S.A., 1993. Catastrophic overturn of the Earth's mantle driven by multiple phase changes and internal heat generation, *Geophys. Res. Lett.*, **20**, 101–104.

Weinstein, S.A. & Olson, P., 1990. Planforms in thermal convection with internal heat sources at large Rayleigh and Prandtl numbers, *Geophys. Res. Lett.*, **17**, 239–242.

Weinstein, S.A., Olson, P.L. & Yuen, D.A., 1989. Time-dependent large aspect-ratio thermal convection in the Earth's Mantle, *Geophys. astrophys. Fluid Dyn.*, **47**, 157–197.

White, D.B., 1988. The planforms and onset of convection with a temperature-dependent viscosity, *J. Fluid Mech.*, **191**, 247–286.

Whitehead, J.A. & Parsons, B., 1978. Observations of convection at Rayleigh numbers up to 760,000 in a fluid with large Prandtl number, *Geophys. astrophys. Fluid Dyn.*, **9**, 201–217.

Yuen, D.A., Hansen, U., Zhao, W., Vincent, A.P. & Malevsky, A.V., 1993. Hard turbulent thermal convection and thermal evolution of the mantle, *J. geophys. Res.*, **98**, 5355–5373.